Article type : Original Article

Ultrasound Imaging based on Molecular Targeting for Quantitative Evaluation of Hepatic Ischemia Reperfusion Injury

Chen Qiu[ab1], Tinghui Yin[ab1], Yingcai Zhang[bc], Yufan Lian[ab], Yujia You[ab], Kun Wang[d], Rongqin Zheng[ab*], Xintao Shuai[ef**]

a Department of Medical Ultrasound, The Third Affiliated Hospital of Sun Yat-sen University, Guangzhou 510630, China.

b Guangdong Key Laboratory of Liver Disease Research, The Third Affiliated Hospital of Sun Yat-sen University, Guangzhou 510630, China.

c Department of Liver Transplantation, The Third Affiliated Hospital of Sun Yat-sen University, Guangzhou 510630, China.

d Key Laboratory of Molecular Imaging, Institute of Automation, Chinese Academy of Science, Beijing 100190, China.

e PCFM Lab of Ministry of Education, School of Chemistry and Chemical Engineering, Sun Yat-sen University, Guangzhou 510275, China.

f Center for Biomedical Engineering, Zhongshan School of Medicine, Sun Yat-sen University, Guangzhou 510275, China.

This article has been accepted for publication and undergone full peer review but has not been through the copyediting, typesetting, pagination and proofreading process, which may lead to differences between this version and the Version of Record. Please cite this article as doi: 10.1111/ajt.14345

*Correspondence to Rongqin Zheng, Department of Medical Ultrasound, The Third Affiliated Hospital of Sun Yat-sen University, Guangzhou 510630, China. E-mail addresses: zhengrq@mail.sysu.edu.cn (R Zheng)
**Correspondence to Xintao Shuai, PCFM Lab of Ministry of Education, School of Chemistry and Chemical Engineering, Sun Yat-Sen University, Guangzhou 510275, China. shuaixt@mail.sysu.edu.cn (X. Shuai).

These authors contributed equally to this work.

Running Title: Targeted ultrasound imaging for hepatic IRI

Abbreviations:

IRI = ischemia reperfusion injury

US = ultrasound

CEUS = contrast-enhanced ultrasound

MB = microbubble

VEGFR2 = vascular endothelial growth factor receptor 2

ICAM-1 = intracellular adhesion molecule 1

MB_{ICAM-1} = ICAM-1 targeted microbubble

MB_{CON} = control microbubble

NID = normalized intensity difference

AST = serum alanine aminotransferase

ALT = aspartate transaminase

2D = two-dimensional

3D = three-dimensional

CLSM = confocal laser scanning microscopy

ROI = region of interest

Abstract

The present study aimed to quantitatively diagnose and monitor the therapy response of hepatic ischemia reperfusion injury (IRI) with targeted ultrasound (US) imaging. Targeted microbubbles (MB_s) were fabricated, and the binding of ICAM-1 antibodies to MBs was observed. To establish a quantitative method based on targeted US imaging, contrast-enhanced ultrasound (CEUS) was applied on IRI rats. After andrographolide treatment, the IRI rats were subjected to the quantitative targeted US imaging for a therapeutic effect. Effective binding of ICAM-1 antibodies to MBs was observed. According to the quantitative targeted US imaging, the ICAM-1 normalized intensity difference (NID) in IRI rats (38.74 ± 15.08%) was significantly higher than that in the control rats (10.08 ± 2.52%, $P = 0.048$). Furthermore, different degrees of IRI (mild IRI, moderate to severe IRI) were distinguished by the use of NID (37.14 ± 2.14, 22.34 ± 1.08, $P = 0.002$). Analysis of mRNA expression demonstrated the accuracy of analyzing the NID using quantitative targeted US imaging ($R^2 = 0.7434$, $P < 0.001$). Andrographolide treatment resulted in obviously weakened NID of ICAM-1 (17.7 ± 4.8% *vs* 34.2 ± 6.6%, $P < 0.001$). The study showed the potential of the quantitative targeted US imaging method for the diagnosis and therapeutic monitoring of IRI.

Introduction

Hepatic ischemia reperfusion injury (IRI) represents the most significant physiopathologic condition characterized by extensive inflammatory changes and is a major cause of mortality and morbidity after liver transplantation or major hepatic resections (1-3). IRI consists of the primary injury from an ischemic condition and further injury once blood

supply is restored (4). The injury severity of the liver parenchyma ranges from moderately raised levels of serum aminotransferases to primary non-function or initial poor graft function, which is associated with many factors following liver transplantation, such as intrahepatic and/or extrahepatic nonanastomotic biliary strictures (5-6). IRI therapies are being extensively investigated due to a lack of available treatment in clinics to date (7). Unfortunately, despite the urgent need for palliative therapy, clinical trials may not be initiated unless optimal treatment effects can be precisely evaluated.

Currently, pathological and biochemical examinations are widely used in both IRI diagnosis and treatment. Although pathological examination is regarded as the goldern standard, it is an invasive procedure and only provides semi-quantitative information. In contrast, a biochemistry test revealing serological changes is not able to show morphology or pathological changes. Thus, a method capable of visualizing inflammation during IRI in a noninvasive and quantitative manner could provide precise information for early diagnosis and monitoring therapeutic effects of the disease in preclinical research (8-10).

Targeted ultrasound (US) imaging has been newly developed to characterize and measure biological processes at the cellular and molecular levels (11, 12), which combines the advantages of excellent sensitivity and specificity of contrast-enhanced ultrasound (CEUS). So far, targeted US imaging has shown good safety and accuracy in multiple preclinical trials (13, 14), and moreover, it has even been applied in human clinical research on neoangiogenesis with vascular endothelial growth factor receptor 2 (VEGFR2) targeted US imaging in various cancer types (15). For targeted US imaging, gas-containing contrast MBs based on liposomes are the most common probes functionalized with targeting ligands

that specifically bind to particular molecular markers (11, 14). Furthermore, intracellular adhesion molecule 1 (ICAM-1) is known as a major inflammatory molecule during IRI and is highly involved in the neutrophil rolling, adhesing, diapedesis, and tissue infiltration during IRI (3). Considering its abundant expression at the hepatic sinusoidal endothelium at a very early stage after IRI, ICAM-1 could be an ideal target for designing targeted microbubbles (MB). To quantify molecular ligand-attached contrast MB, a typical destruction-replenishment regimen (Schematic diagram) was employed in most of the current preclinical studies on targeted US imaging (16-19). ICAM-1 targeted US imaging could be a promising quantitative technology enabling accurate detection and therapeutic monitoring IRI at the molecular level.

The present study aimed to precisely diagnose and monitor the therapy response of hepatic IRI with quantitative targeted US imaging.

Materials and methods

All animals in the research were treated according to the guidelines issued by the Sun Yat-sen University Animal Care Committee. The manuscript has been read and approved by all authors.

Preparation of MBs and in vitro specific binding experiment

Two types of MBs (ICAM-1 targeted MBs, MB_{ICAM-1} and control MBs, MB_{CON}) were prepared. The diameters of each MB were determined. *In vitro* experiments assessed the conjunction of ICAM-1 to the surface of MBs and specific binding efficacy of MB_{ICAM-1} to ICAM-1. See supporting information [online] for details about the *in vitro* assessment.

Animal models

Male Sprague-Dawley rats weighing 270-300 g were acclimatized under the standard laboratory conditions at Sun Yat-sen University for one week. All animals were kept in a temperature and humidity controlled room and divided into 3 groups to establish a quantitative targeted US imaging method: control group (n = 6), mild IRI group (n = 6), moderate to severe IRI group (n = 12). In the IRI groups, the rats received hepatic IRI surgery as follows: rats were fasted 18 hours before the experiments but were fed with water. Under pentobarbital sodium (30 mg/kg, i.p.) anesthesia, the portal vein, hepatic artery and bile duct were clamped to induce a complete ischemia condition of the liver. After 20 or 30-40 minutes of the ischemia procedure, the clip around the vessels was removed to allow reperfusion, which led to mild IRI models or moderate to severe IRI models. In the control group, the rats received a sham operation: 30 minutes after anesthesia and laparotomy without clamping the portal vein, hepatic artery and bile duct, the abdomens of the rats were closed. After 24 hours of reperfusion or sham operation, CEUS was performed, and small amounts of blood (0.4 ml) and liver tissues were collected after the animals were sacrificed (Fig 1). See supporting information [online] for details about the modeling evaluation.

Targeted US imaging of ICAM-1

CEUS was performed according to the supporting information. Based on a clinical US imaging system (Logiq E9 digital premium ultrasound system, GE, USA), images of the rat liver were collected using a broadband ML6-15D high-frequency with imaging parameters as follows: frequency of 10 MHz; gain of 20-40 dB; image depth of 2-3 cm; AO% of 100%; dynamic range of 69 dB; mechanical index of 0.07 at first porta hepatic plane of the liver

section. Targeted US imaging was obtained *via* a destruction-replenishment approach (Sigma plot): after 60 seconds of continuous imaging of sufficiently bond and free MBs, all MBs in the sector were destroyed by increasing the mechanical index from 0.07 to 0.24 for 1 second by setting a "flash" function. Subsequent post-destruction images lasted for 10 seconds to capture freely circulating MBs.

To demonstrate specific binding of MB_{ICAM-1} to the injured hepatic sinusoidal endothelium *in vivo*, two groups of animals were investigated: a control group (n = 3) and IRI group (e.g., moderate to severe IRI models, n = 3). 50 μl of MB_{CON} in PBS with a bubble concentration of 2.0×10^7 bubbles/ml was injected *via* the tail vein. To allow clearance of MB_{CON}, MB_{ICAM-1} with the same concentration and volume was applied to the rat 1 hour after the previous injection. After the injection of each type of MB, a US imaging sequence using a destruction-replenishment approach was performed as described previously.

Establishment of quantitative targeted US imaging

A control group (n = 6), mild IRI group (n = 6), and moderate to severe IRI group (n = 12) were included. An offline analysis in random order was performed for all imaging data. A quantitative targeted US imaging signal from MBs that bonded to ICAM-1 was determined using the CEUS quantitative analyzing software Sonamath (AmbitionT.C., China). Imaging of the regions of interest (ROI) was performed using pre-destruction contrast frames representing both the attached and free MBs and post-destruction contrast frames representing only the freely circulating MBs. The imaging signal from the attached MBs was calculated by subtracting the post-destruction signal from the pre-destruction one. The quantification of imaging signal was achieved using normalized intensity differences

(NID, %). In other words, the ratio of the attached MBs imaging signal intensity to the total MBs imaging signal intensity was calculated. Images representing the attached MB were displayed as a color-coded signal overlapped with the B-mode image. A linear regression analysis was conducted to access the correlation between *ex vivo* expression levels of ICAM-1 mRNA and *in vivo* NID.

Monitoring of anti-inflammatory treatment

As for monitoring experiments, an additional 6 rats receiving IRI surgery (e.g., moderate to severe IRI rats) were treated with an anti-inflammatory drug. Briefly, andrographolide (1 mg/kg; Sigma, St. Louis, MO) dissolved in 2% dimethyl sulfoxide (DMSO) was added in 0.1 ml saline and administered by intraperitoneal injections 2 hours before the hepatic ischemia procedure and immediately before reperfusion. After 24 hours of reperfusion, the *in vivo* quantitative targeted US imaging method was utilized to monitor treatment efficacy. The procedure was the same as described previously. Additionally, some regular examinations were also employed to evaluate anti-inflammatory treatment as described in the animal modeling section.

Statistical analysis

All experiments were repeated at least 3 times, and the data were analyzed using Student's t tests or one-way ANOVA analysis (SPSS software, version 13.0, SPSS Inc.). Unless otherwise specified, data were expressed as the means ± standard deviation. A linear regression analysis was applied to access the correlation between *ex vivo* expression levels of ICAM-1 mRNA and *in vivo* NID. Moreover, the determination correlation coefficient (R^2) was calculated to access goodness of fit between these two variables. To determine the

accuracy of NID in treated animals, Pearson's linear analysis was applied between the actual intensity difference and the value estimated by the correlation equation. The correlation coefficient (r) was acquired to identify the correlation degree. A $P < 0.05$ was considered significant.

Results

Characterization of MB_{ICAM-1}

According to the DLS measurements, the average diameter of MB_{ICAM-1} was 1.2 ± 0.1 μm, similar to that of MB_{CON} (1.1 ± 0.2 μm). This result indicated that conjugation of ICAM-1 antibodies did not significantly affect particle size. In this study, MB_{ICAM-1} was prepared with an improved maleimide-thiol method, which increased the preparation efficiency (Fig S1).

For the confocal laser scanning microscopy (CLSM) study, the DiI probe was encapsulated to make the MBs visible, and FITC-labeled secondary antibody was used to trace ICAM-1 antibody. As shown in Fig 2, the red and green fluorescence almost overlapped, indicating successful conjugation of ICAM-1 antibody to MBs.

ICAM-1 targeted US imaging and quantitative analysis

To gain targeted CEUS imaging, MB_{ICAM-1} or MB_{CON} was injected *via* the tail vein to the rats. Upon receiving MB_{ICAM-1}, a much stronger molecular US imaging signal was observed in the IRI group compared with that of the control group (Fig 3A). Additionally, a greater signal intensity in the IRI group was shown *via* administration of MB_{ICAM-1} compared to MB_{CON} (Fig 3A), confirming the specificity of MB_{ICAM-1} to IRI-liver. The NID

was adopted as a parameter for further quantitative analysis of ICAM-1 targeted US imaging. After administration of $MB_{ICAM-1,}$ there was a significant difference (P = 0.048) in NID between the IRI animals (38.74 ± 15.08%) and control rats (10.08 ± 2.52%), which accorded well with the results of targeted US imaging. In contrast, no significant difference in NID was noted between the IRI and control animals (8.03 ± 3.00% and 12.58 ± 2.66%, P = 0.319) after administration of MB_{CON} (Fig 3B).

ICAM-1 targeted US imaging was further applied to distinguish different degrees of IRI (mild IRI, moderate to severe IRI). After administration of MB_{ICAM-1}, the imaging signal was strongest in the moderate to severe IRI group and weaker in the mild group (Fig 4). Consistently, NID was significantly highest in the moderate to severe IRI group (37.14 ± 2.14) compared with that of the mild IRI group (22.34 ± 1.08, P = 0.002). The NIDs of both the moderate to severe IRI group and mild IRI group were much higher than that of control IRI (15.77 ± 0.91, P < 0.001 moderate to severe IRI group vs control group, P = 0.009 mild group *vs* control group) (Fig 4). With the subjection of ICAM-1 targeted US imaging, different levels of IRI were successfully identified.

Moreover, to verify the accuracy of quantitative targeted US imaging results, relative mRNA expression of ICAM-1 was measured to represent the pathological status at the molecular level. A linear regression equation regarding NID and mRNA expression level was established (Y = 1.11 X – 9.5323, where X and Y are NID and ICAM-1 mRNA expression respectively, P < 0.001). The coefficient (R^2), which represented the determined degree of NID relative to ICAM-1 mRNA expression, reached as high as 0.7434 (Fig 5), and R^2, analyzed with the conventional subtracted value, was only 0.3012. Apparently, NID

corresponding to ICAM-1 mRNA expression was reflected much more clearly in our improved method compared with the conventional way in which intensity difference was expressed as a simple subtraction. As the pathological result was regarded as the golden diagnosing standard, the accuracy of our quantitative data was verified by the significant correlation between the NID and molecular biological results, which laid the foundation for quantitative diagnosing and monitoring of IRI-liver.

Monitoring of anti-inflammatory treatment

The anti-inflammatory efficacy was estimated after andrographolide intraperitoneal treatment.

Monitoring of anti-inflammatory effect by conventional method The serum AST and ALT activities indicating hepatocellular damage after liver IRI decreased significantly ($P < 0.001$ and $P = 0.035$, respectively) in IRI rats receiving andrographolide treatment (571.8 ± 159.8 U/L and 192.8 ± 104.6 U/L, respectively) compared with animals without treatment (1336.3 ± 296.1 U/L and 356.7 ± 127.7 U/L, respectively) (Fig 6A and Fig 6B). As ICAM-1 was stimulated on endothelial cells as a consequence of inflammation response after IRI, ICAM-1 expression at the mRNA level measured by RT-PCR indicated the severity of IRI. Indeed, ICAM-1 expression at the mRNA level decreased significantly (5.3 ± 2.9% *vs* 26.7 ± 15.6%, $P = 0.008$) (Fig 6C). Similarly, ICAM-1 immunohistochemical staining studies showed the same trend of mRNA levels. Specifically, ICAM-1 protein expression in treated animals was also weaker than that in IRI animals (Fig 6F). Additionally, pathological changes observed by H&E staining in the IRI liver showed some unclear hepatic cord structures, sinusoidal congestion and hepatocytes with karyopyknosis and swelling, etc. In

comparison, no obvious signs of these symptoms were identified in the treated IRI liver (Fig 6E). Suzuki's score on the basis of H&E staining was significantly lower in the treated group than that in the IRI group (0.93 ± 0.1 *vs* 2.2 ± 0.4, $P < 0.001$) (Fig 6D). All these results demonstrated the anti-inflammation effects of andrographolide for IRI by inhibiting ICAM-1 expression.

Monitoring of anti-inflammatory effect using targeted US imaging After IRI surgery, animals in the treated group received targeted US imaging of ICAM-1 by injecting MB_{ICAM-1} via the tail vein. The ICAM-1 targeted US imaging signal (Fig 7A) in rats treated with andrographolide was weaker than that in the untreated animals (Fig 7B), which was consistent with other evidence of anti-inflammatory effects including serum indicators and pathological examinations after andrographolide treatment. Further quantitative analysis of targeted US imaging (Fig 7D) using NID was then conducted to show the anti-inflammatory efficacy of andrographolide as well. NID decreased to 17.7 ± 4.8% from 34.2 ± 6.6% after treatment ($P < 0.001$), indicating less inflammation. ICAM-1 mRNA expression in the treated group was also detected, and then, NID was estimated using the equation: $Y = 1.11\ X - 9.5323$ (where X and Y represent NID and ICAM-1 mRNA expression, respectively). Finally, Pearson's linear analysis was applied in the treated group between NID estimated and obtained from targeted US imaging, respectively. The two quantitative data points were very close (a correlation coefficient $r = 0.828$, $P = 0.042$), which strongly demonstrated the accuracy of our quantitative method using ICAM-1 US imaging to monitor anti-inflammatory treatment in IRI animal models.

Discussion

IRI is known as a major cause of mortality for patients after liver transplantation (1- 3). Considering the available diagnosis methods for IRI with either invasive risk or non-specific limitations (4, 5), it is anticipated that a noninvasive and quantitative approach to access the severity of hepatic IRI would further encourage the robust studies in IRI treatment. Targeted US imaging meets such a need by the combination of a noninvasive modality and quantitative evaluation method at the molecular level. Hence, targeted US imaging possesses great potential for early assessment of treatment effects. Although targeted US imaging has been employed thus far in monitoring various diseases such as inflammatory diseases, cardiovascular diseases and tumors (16, 20, 21), it has not been investigated in hepatic IRI. In the present study, targeted US imaging was employed for this disease as a quantificational and specific monitoring tool.

Because MBs would stay within the vascular compartments due to their large sizes (several micrometers in general), the ideal targets for US imaging should be the molecules on the luminal surface (15). For IRI, these molecules include ICAM-1, vascular adhesion molecule (VCAM) and selectins, all of which play critical roles mediating the rolling of leucocytes on the vascular endothelium, leading to firm adhesion and diapedesis of leucocytes at sites of tissue injury and inflammation (22-25). Among the molecules, ICAM-1 is known as a major inflammatory molecule that reaches its highest expression level 24 hours after reperfusion, which is an appropriate time frame for applying targeted US imaging (3, 23). Therefore, targeted US imaging was conducted based on the detection of ICAM-1 US imaging signals during IRI. The technique that we proposed in the study could be extended to

studies using other targets (such as VCAM, P-selectin) to evaluate IRI at various phases.

As targeted contrast agents were the basis of targeted US imaging (14), we designed an MB conjugating $scFv_{ICAM-1}$ with an improved maleimide-thiol conjugation method. Compared with the conventional method which fabricated MB first and then linked antibodies (26, 27), our approach which linked antibodies first but fabricated MB later effectively reduced the loss of targeted MBs and thus enhanced the output. Details are shown in the supporting information [online].

Moreover, aiming at acquiring quantitative targeted US imaging signal of IRI, the destruction-replenishment method utilized in this study was improved. Several studies have used the traditional approach to define the quantitative targeted US imaging signal as the absolute subtraction value of imaging signal pre- and post-destruction (conventional method) (16-19). However, slight deviations may occur because the absolute value was not able to exclude influences of tissue attenuation and system settings. A ratio of quantification could address those problems (28). In Wang's study using an acute terminal ileitis model (28), the Intensity Ratio was defined as the ratio of the imaging signal amplitudes before to after destruction (Intensity Ratio = image signal before destruction / image signal post destruction) to quantify targeted US imaging (28). In contrast, in the present study, NID [NID = image signal before destruction - image signal post destruction / image signal before destruction] was employed to gain quantitative targeted US imaging. In a destruction-replenishment method, the exact targeted US imaging signal intensity should be the subtraction of the imaging signal after destruction from that before destruction (Sigma plot). Therefore, our method using NID based on a signal intensity subtraction is believed to be more appropriate

for quantitative imaging in the destruction-replenishment method, which is different from Wang's method using Intensity Ratio to emphasize magnification of the imaging signal before destruction to that after destruction.

ICAM-1 NID were significantly higher in IRI rats (38.74 ± 15.08%) than in normal rats (10.08 ± 2.52%), which directly indicated more severe inflammatory changes in IRI rats. Considering that the quantitative targeted US imaging results in other studies often lacked evidence to show good consistency with the admitted golden standard, we further introduced a linear correlation analysis between the quantitative result (ICAM-1 NID) and pathological molecular level (ICAM-1 mRNA expression). As expected, the values of ICAM-1 NID varied against ICAM-1 mRNA expression linearly ($R^2 = 0.7434$, $P < 0.001$), which provided strong evidence of the reliability of the quantitative data based on targeted US imaging.

The use of our quantitative targeted US imaging method to monitor anti-inflammatory treatment was then evaluated in IRI rats. A drug, andrographolide, was confirmed to effectively reduce IRI inflammation. Andrographolide is a labdane diterpene lactone isolated from the leaves of the andrographis paniculata plant, which has shown hepatocyte-protective and anti-inflammatory activities in many diseases (29- 31). However, its anti-inflammatory effect of IRI has never been demonstrated. In this study, we observed a significant anti-inflammatory effect of andrographolide on IRI animals as judged from serum test, biochemical test, pathological test and targeted US imaging results. The anti-inflammatory mechanism of andrographolide for IRI may involve ICAM-1 regulation, but more details need to be explored. After treatment, ICAM-1 molecular images were first exported as a relatively quick and convenient qualitative result to monitor anti-inflammation effects.

Subsequently, a quantitative analysis was applied to obtain a more precise result. ICAM-1 NID showed a 16.5% decrease ($P < 0.001$) in inflammation after treatment in IRI rats. Additionally, the data obtained from targeted US imaging and estimated from the previous equation in the treated group showed good accordance in a Pearson's linear analysis ($r = 0.828$, $P < 0.001$). Such quantitative data enabled monitoring of IRI treatment in a more objective and precise manner.

The following limitations should be noted for the present study. First, the quantitative approach using destruction-replenishment allowed separation of imaging signals from targeted and free MBs. A high mechanical index US pulse was conducted to destroy freely circulating MBs, which may lead to unwarranted biological consequences caused by MB-induced cavitation (32). Second, the imaging approach was facilitated by a clinically available two-dimensional (2D) US transducer which has a relatively limited field of view. In comparison, three-dimensional (3D) quantification using phased array 3D ultrasound transducers is more desirable to detect the spatial distribution of molecular marker expressions in targeted tissues for an improved imaging field (33, 34). Third, the detection of ICAM-1 US molecular imaging only presented limited information on phase of IRI. Finally, ICAM-1 mRNA levels, which were used to confirm the reliability of NID, did not exactly reflect ICAM-1 protein expression on the cellular surface.

In conclusion, inflammation of IRI was quantitatively assessed in IRI rats with ICAM-1 targeted US imaging. Moreover, the accuracy and reliability of the improved quantitative targeted US imaging method was confirmed. Using this method, the anti-inflammatory treatment effect of andrographolide in rats with IRI was monitored successfully, which

showed that this drug may provide a new IRI therapy. This study indicates that the new targeted US imaging strategy may facilitate clinical trials of IRI US diagnosis and therapeutic monitoring.

Acknowledgments

This work was supported by the National Natural Science Foundation of China (Grant Nos. 8143000314, 81271577, U1401242, 81500501, 81601512).

Disclosure

The authors of this manuscript have no conflicts of interest to disclose as described by the American Journal of Transplantation.

Figure legends

Sigma plot. Schematic diagram shows principles of destruction-replenishment method for quantification targeted US imaging. (A) Several minutes following intravenous administration, signals from molecularly attached MBs and freely circulating MBs of targeted tissue were obtained as the first US data. Following a high-powered US pulse to destroy both attached and freely circulating MBs within the beam elevation of the US transducer, a second US data set is acquired at several seconds after the destruction pulse to allow freely circulating MBs to replenish into the imaging plane. (B) Calculation method of destruction/replenishment method. The US imaging signal from MBs attached to the molecular target is expressed as the subtraction of MB densities before and after the

destruction pulse. Targeted signal（dB）= MBD_{pre} - MBD_{post}. MBD = MB densities.

Figure 1. Overview of experimental design of *in vivo* targeted US imaging. (A) Establishment of quantitative ICAM-1 US imaging method. (B) Monitoring anti-inflammatory effect after andrographolide treatment using quantitative ICMA-1 US imaging. IRI = ischemia reperfusion injury. Both hepatic IRI rats and those with treatment followed the same surgical procedure: underwent the ischemia procedure at the 0 hour point and underwent the reperfusion procedure at the 0.5 hour point.

Figure 2. Observation of structures of MB_{ICAM-1} using laser confocal scanning microscopy (LCSM, 20×): (A) The lipid shell of MB was stained with DiI. (B) FITC labeled secondary antibodies were used to locate ICAM-1 antibodies. (C) White field images. (D) Merged images. Red fluorescence: MB_s stained with DiI; Green fluorescence: ICAM-1 secondary antibodies labeled FITC.

Figure 3. (A) Representative targeted US images of MB_{ICAM-1} and MB_{CON} in IRI rats and control rats. US signal after MB_{ICAM-1} in IRI liver was substantially higher than that in control liver and was significantly higher compared with MB_{CON} in IRI liver and normal liver. (B) NIDs were calculated as the ratio of subtraction using the destruction-replenishment method. (n = 3, $*P = 0.048$, IRI group compared with control group after MB_{ICAM-1} administration).

Figure 4. The graph summarizes the correlation analysis between ICAM-1 NID and relative ICAM-1 mRNA expression in the livers of both IRI and normal rats. The two variables had a linear correlation with a coefficient of determination $R^2 = 0.7434$, $P < 0.001$.

Figure 5. Representative targeted US images evaluating different degrees of IRI. Targeted US imaging signal was weakest in the control liver (A) and strongest in the moderate to severe IRI liver (C) compared to that in the mild IRI liver (B). (D) NID in each group. ($^*P < 0.001$ mild IRI group *vs* control group, $^{\#}P = 0.002$ moderate to severe IRI group *vs* mild IRI group, $^{\&}P < 0.001$ moderate to severe IRI group *vs* control group).

Figure 6. Evidence of anti-inflammatory efficacy after treatment. (A) AST activity (n = 6, $^*P < 0.001$ IRI group *vs* control group, $^{\#}P < 0.001$ treated group *vs* IRI group). (B) ALT activity (n = 6, $^*P < 0.001$ IRI group *vs* control group, $^{\#}P = 0.035$ treated group *vs* IRI group). (C) Relative mRNA expression of ICAM-1 in liver tissues determined by RT-PCR (n = 6, $^*P = 0.040$ IRI group *vs* control group, $^{\#}P = 0.008$ treated group vs IRI group). (D) Suzuki's score of each group (n = 6, $^*P < 0.001$ IRI group *vs* control group, $^{\#}P < 0.001$ treated group *vs* IRI group). (E) H&E staining of liver tissues. Arrows present variations of sinusoidal congestion and hepatocytes with swelling in the IRI group (magnification: 100× or 400×). (F) Protein expression level of ICAM-1 determined by immunohistochemistry of liver tissues (magnification: 100× or 400×).

Figure 7: Representative targeted US images evaluating anti-inflammatory efficacy. Targeted US imaging signal was weaker in the control liver (A) and treated IRI liver (C) than in the non-treated (B) IRI liver. (D) NID in each group. (*$P < 0.001$ IRI group *vs* control group, $^{\#}P < 0.001$ treated group *vs* IRI group).

Supporting Information

Additional Supporting Information may be found in the online version of this article.

Supplemental Materials and Methods

Figure S1: The output efficacy of MB_{ICAM-1} prepared with novel and traditional methods. (A): General observation of MB_{ICAM-1} in vials. The left showed higher MB concentration achievable with the present method, and the right showed lower MB concentration with the traditional method. Observation of MB_{ICAM-1} under microscope (100×); (B) prepared with present method; (C) with traditional method. Both types of MB_{ICAM-1} appeared single, dispersive and spherical. However, more abundant MBs were observed with the present method.

Figure S2：Observation of specific attachment of MB_{ICAM-1} to C6 cells using fluorescence microscopy (magnification, 200×). Blue fluorescence: nuclei stained with Hoechst 33342; Red fluorescence: both MB_{ICAM-1} and MB_{CON} stained with DiI. Bar stands for 100 μm.

Figure S3: Hepatic IRI models of rats: (A) AST activity (n = 6, *$P < 0.001$ mild IRI group *vs* control group, $^{\#}P < 0.001$ moderate to severe IRI group *vs* mild IRI group, $^{\&}P < 0.001$

moderate to severe IRI group *vs* control group). (B) ALT activity (n = 6, $^{*}P = 0.001$ mild IRI group *vs* control group, $^{\#}P = 0.002$ moderate to severe IRI group *vs* mild IRI group, $^{\&} P < 0.001$ moderate to severe IRI group *vs* control group). (C) Relative mRNA expression of ICAM-1 in liver tissues determined by RT-PCR (n = 6, $^{*}P = 0.006$ mild IRI group *vs* control group, $^{\#}P = 0.015$ moderate to severe IRI group *vs* mild IRI group, $^{\&}P < 0.001$ moderate to severe IRI group *vs* control group). (D) Suzuki's score of each group (n = 6, $^{*}P = 0.003$ mild IRI group *vs* control group, $^{\#}P < 0.001$ moderate to severe IRI group *vs* mild IRI group, $^{\&}P < 0.001$ moderate to severe IRI group *vs* control group).

References:

1. Saidi RF and Kenari SK. Liver ischemia/reperfusion injury: an overview. J Invest Surg. 2014. 27(6): p. 366-79.
2. Eltzschig HK and Eckle T. Ischemia and reperfusion-from mechanism to translation. Nature Medicine. 2011. 17(11): p. 1391-1401.
3. Peralta C, Jimenez-Castro MB and Gracia-Sancho J. Hepatic ischemia and reperfusion injury: effects on the liver sinusoidal milieu. J Hepatol. 2013. 59(5): p. 1094-106.
4. Cursio R, Colosetti P and Gugenheim J. Autophagy and Liver Ischemia-Reperfusion Injury. BioMed Research International. 2015. 2015: p. 1-16.
5. Cursio R and Gugenheim J. Ischemia-Reperfusion Injury and Ischemic-Type Biliary Lesions following Liver Transplantation. Journal of Transplantation. 2012. 2012: p. 1-17.
6. Glanemann M, Langrehr JM., Stange BJ, Neumann U, Settmacher U, Steinmu¨ ller T and Neuhaus P. Clinical Implications of Hepatic Preservation Injury After Adult Liver Transplantation. Am J Transplant. 2003. 3:p1003-1009.
7. Jaeschke, H and Woolbright BL. Current strategies to minimize hepatic ischemia–reperfusion injury by targeting reactive oxygen species. Transplantation Reviews. 2012. 26(2): p. 103-114.
8. Palmowski M, Huppert J, Ladewig G, Hauff P, Reinhardt M,. Mueller MM, et al. Molecular profiling of angiogenesis with targeted ultrasound imaging: early assessment of antiangiogenic therapy effects. Molecular Cancer Therapeutics. 2008. 7(1): p. 101-109.
9. Kiessling F, Fokong S, Koczera P, Lederle W, Lammers T. Ultrasound microbubbles for molecular diagnosis, therapy, and theranostics. J Nucl Med. 2012. 53(3): p. 345-8.
10. Leong-Poi H, Christiansen J, Heppner P, Lewis CW, Klibanov AL, Kaul S, Lindner JR. Assessment of endogenous and therapeutic arteriogenesis by contrast ultrasound molecular imaging of integrin expression. Circulation. 2005. 111(24): p. 3248-54.
11. Unnikrishnan S, Klibanov AL. Microbubbles as ultrasound contrast agents for

molecular imaging: preparation and application. AJR Am J Roentgenol. 2012. 199(2): p. 292-9.
12. Jokerst JV and Gambhir SS. Molecular imaging with theranostic nanoparticles. Acc Chem Res. 2011. 44(10): p. 1050-60.
13. Kiessling F, Fokong S, Bzyl J, Lederle W, Palmowski M, Lammers T. Recent advances in molecular, multimodal and theranostic ultrasound imaging. Adv Drug Deliv Rev. 2014. 72: p. 15-27.
14. van Rooij T, Daeichin V, Skachkov I, de Jong N, Kooiman K. Targeted ultrasound contrast agents for ultrasound molecular imaging and therapy. Int J Hyperthermia. 2015. 31(2): p. 90-106.
15. Abou-Elkacem L, Bachawal SV, Willmann JRK. Ultrasound molecular imaging: Moving toward clinical translation. European Journal of Radiology. 2015. 84(9): p. 1685-1693.
16. Kaufmann BA, Sanders JM, Davis C, Xie A, Aldred P, Sarembock JJ, et al. Molecular Imaging of Inflammation in Atherosclerosis With Targeted Ultrasound Detection of Vascular Cell Adhesion Molecule-1. Circulation. 2007. 116(3): p. 276-284.
17. Deshpande N, Lutz AM, Ren Y, Foygel K, Tian L, Scheider M, et al. Quantification and monitoring of inflammation in murine inflammatory bowel disease with targeted contrast-enhanced US. Radiology. 2012. 262(1): p. 172-80.
18. Deshpande N, Ren Y, Foygel K, Rpsenberge J, Willman JK. Tumor angiogenic marker expression levels during tumor growth: longitudinal assessment with molecularly targeted microbubbles and US imaging. Radiology, 2011. 258(3): p. 804-11.
19. Wu J, Leong-Poi, Bin J,Yan L, Liao Y, Liu Y, et al. Efficacy of contrast-enhanced US and magnetic microbubbles targeted to vascular cell adhesion molecule-1 for molecular imaging of atherosclerosis. Radiology, 20
20. Zhang, X, Tian Y, Zhang C, Tian X, Ross, AW, Moir RD, et al., Near-infrared fluorescence molecular imaging of amyloid beta species and monitoring therapy in animal models of Alzheimer's disease. Proceedings of the National Academy of Sciences. 2015. 112(31): p. 9734-9739.
21. Wang X, Hagemeyer CE, Hohmann JD, Leitner E, Armstrong PC, Jia F, et al. Novel Single-Chain Antibody-Targeted Microbubbles for Molecular Ultrasound Imaging of Thrombosis: Validation of a Unique Noninvasive Method for Rapid and Sensitive Detection of Thrombi and Monitoring of Success or Failure of Thrombolysis in Mice. Circulation. 2012. 125(25): p. 3117-3126.
22. Flordeliza SV, Erxiong L, Shivani B, Sevgi K, Eric T, Jianjun W, et al. Myocardial Ischemic Memory Imaging With Molecular Echocardiography. Circulation. 2007. 115(3): p.345–352.
23. Yi Y, Yulin L, Li Y, Juefei W, Jing D, Wanling X , et al. Late-phase detection of recent myocardial ischaemia using ultrasound molecular imaging targeted to intercellular adhesion molecule-1. Cardiovascular Research. 2011. 89:175–183.
24. Charlotte L and Sabine W. ICAM-1 signaling in endothelial cells. Pharmacological Reports. 2009. 61(1): p. 22–32.
25. Beat AK, Christopher L, Aris X, Ayoub MM, and Jonathan RL Detection of recent myocardial ischaemia by molecular imaging of P-selectin with targeted contrast

echocardiography. Eur Heart J. 2007.28(16): p. 2011–2017.
26. Anderson CR, Rychak JJ, Backer M, Backer J, Ley K, Alexander L. scVEGF Microbubble Ultrasound Contrast Agents. Investigative Radiology. 2010. 45(10): p. 579-585.
27. Yeh JS, Sennoga CA, McConnell E, Eckersley R, Tang MX, Nourshargh S, et al. A Targeting Microbubble for Ultrasound Molecular Imaging. PLOS ONE. 2015. 10(7): p. e0129681.
28. Wang H, Felt SA, Machtaler S, Guracar I, Luong R, Bettinger T, et al. Quantitative Assessment of Inflammation in a Porcine Acute Terminal Ileitis Model: US with a Molecularly Targeted Contrast Agent. Radiology. 2015. 276 (3) : 809-17
29. Chen H, Huang CS, Li CC, Lin AH, Huang YJ, Wang TS, Yao HT, et al. Bioavailability of andrographolide and protection against carbon tetrachloride-induced oxidative damage in rats. Toxicology and Applied Pharmacology. 2014. 280(1): p. 1-9.
30. Wang YJ, Wang JT, Fan QX, Geng JG. Andrographolide inhibits NF-kappaBeta activation and attenuates neointimal hyperplasia in arterial restenosis. Cell Res. 2007. 17(11): p. 933-41.
31. Bao, Z, Guan S, Cheng C, Wu S, Wong SH, Kemeny DM, et al., A novel antiinflammatory role for andrographolide in asthma via inhibition of the nuclear factor-kappaB pathway. Am J Respir Crit Care Med. 2009. 179(8): p. 657-65.
32. Abou-Elkacem L, Bachawal SV, Willmann JRK. Ultrasound molecular imaging: Moving toward clinical translation. European Journal of Radiology. 2015. 84(9): p. 1685-1693.
33. Bartolotta, TV, Taibbi Adele, Matranga Domenica, Midiri Massimo, Lagalla Roberto. 3D versus 2D contrast-enhanced sonography in the evaluation of therapeutic response of hepatocellular carcinoma after locoregional therapies: preliminary findings. La radiologia medica. 2015. 120(8): p. 695-704.
34. Naqvi TZ. Quantifying atherosclerosis by "3D" ultrasound works!: But there is work to be done. J Am Coll Cardiol. 2015. 65(11): p. 1075-1077.

Figures and tables

Sigma plot

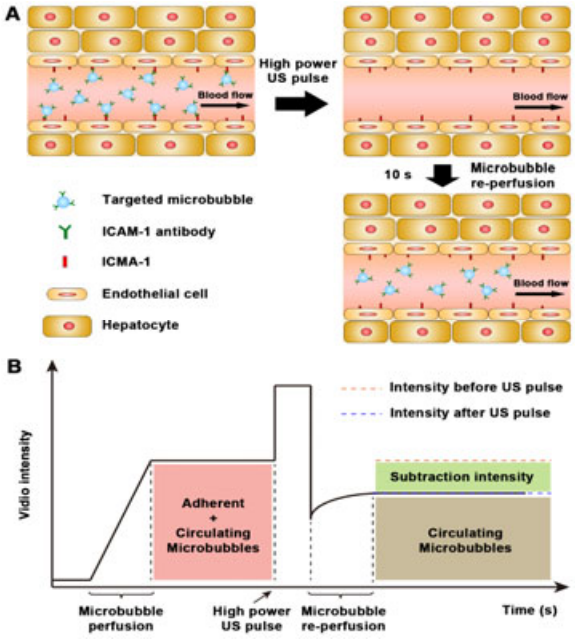

Fig. 1

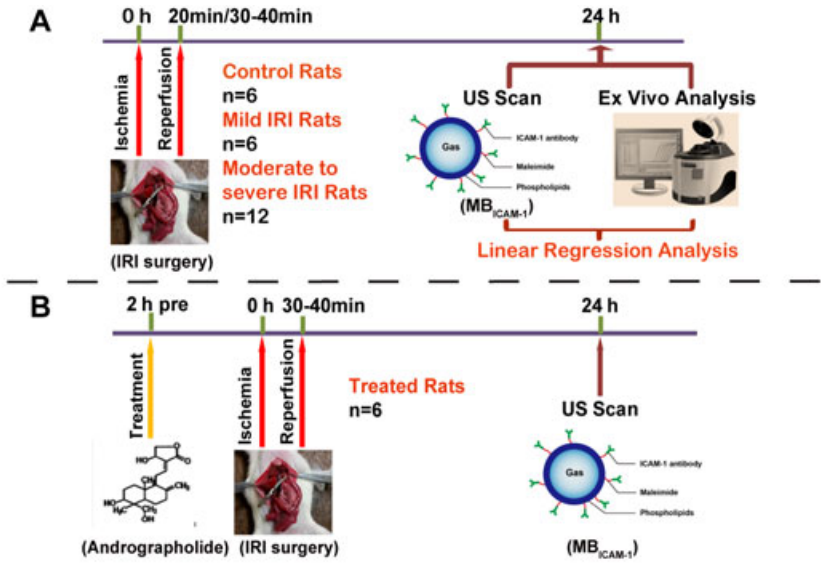

Fig. 2

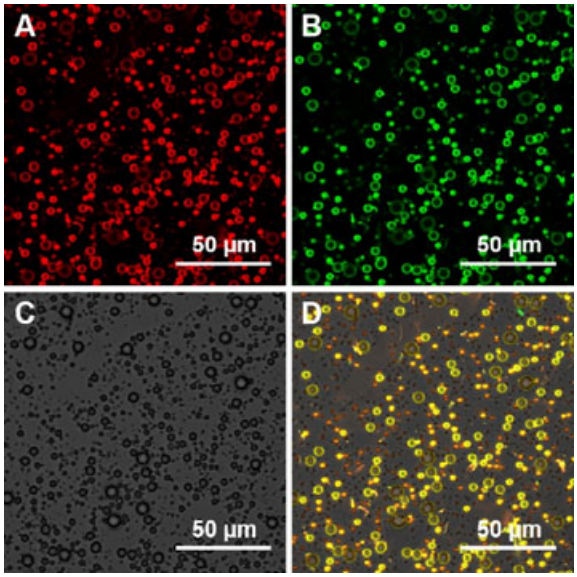

Fig. 3

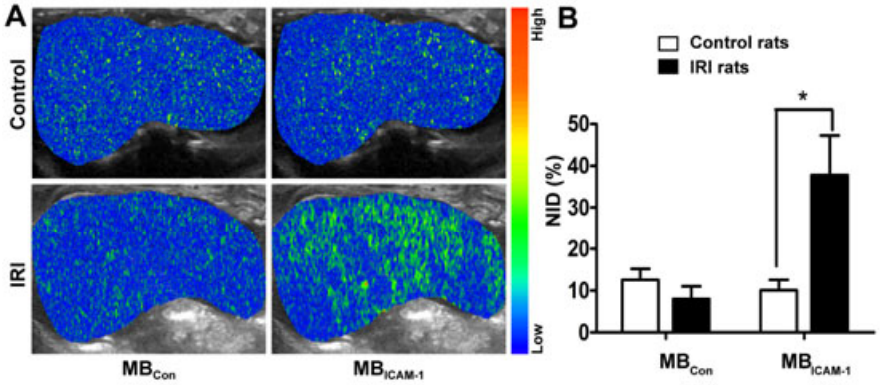

Fig. 4

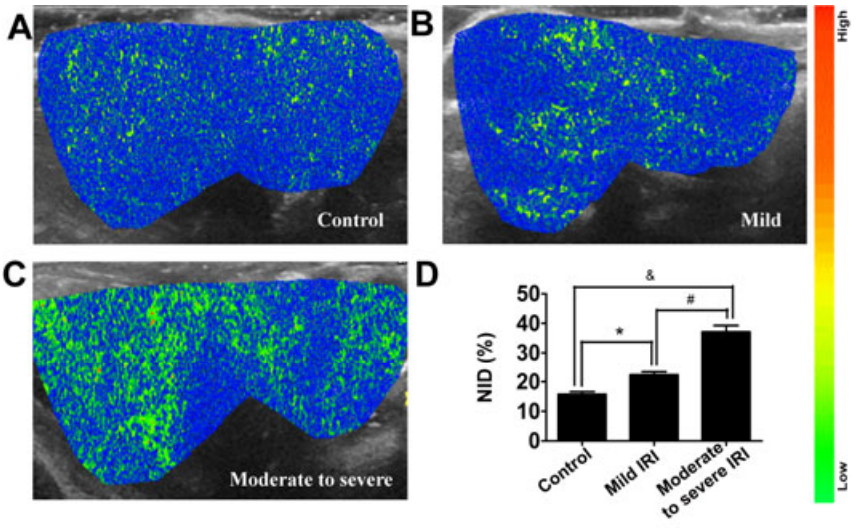

Fig. 5

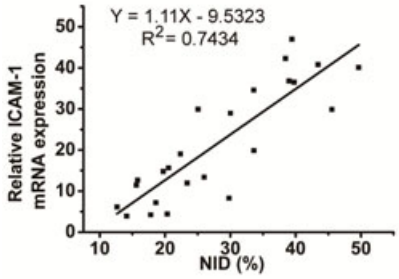

Fig. 6

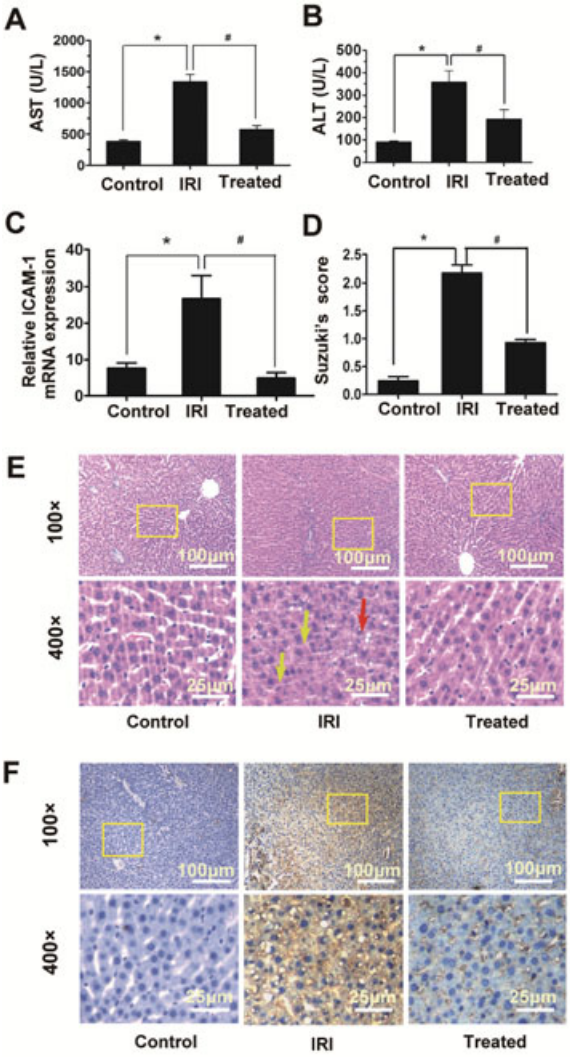

Fig. 7

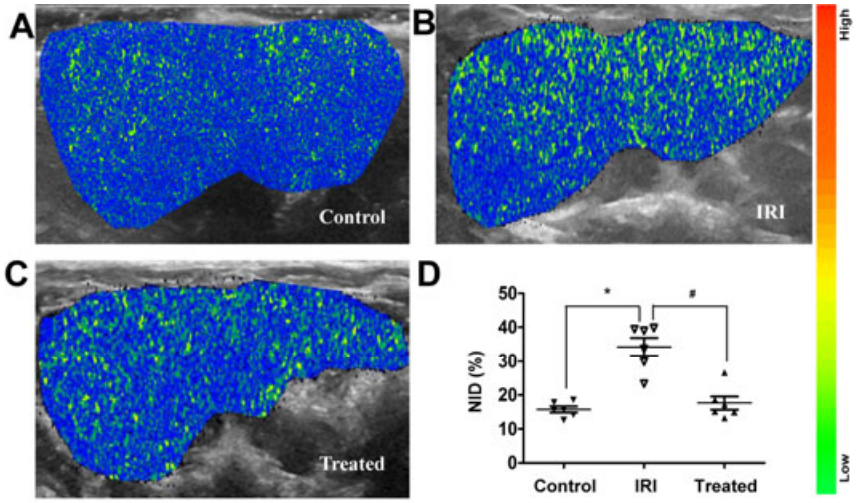

: